Physical and electrochemical evaluation of ATO supported IrO_2 catalyst for proton exchange membrane water electrolyser

Vinod Kumar Puthiyapura [a, *], Mohammed Mamlouk [a], Sivakumar Pasupathi [b], Bruno G. Pollet [b], Keith Scott [a]

[a] School of Chemical Engineering and Advanced Materials, Newcastle University, Newcastle upon Tyne NE1 7RU, United Kingdom
[b] South African Institute for Advanced Materials Chemistry (SAIAMC), Faculty of Science, University of the Western Cape, Private Bag X17, Bellville 7535, South Africa

HIGHLIGHTS

- ATO supported IrO_2 was used as OER catalyst in PEMWE.
- BET surface area of the supported catalysts was predominantly contributed by IrO_2.
- Electronic conductivity of the supported catalyst was predominantly contributed by IrO_2.
- IrO_2 crystallite size in the supported catalyst decreased with IrO_2 loading.
- 40 wt.% reduction of IrO_2 was achieved by utilising support material.

ARTICLE INFO

ABSTRACT

Antimony doped tin oxide (ATO) was studied as a support material for IrO_2 in proton exchange membrane water electrolyser (PEMWE). Adams fusion method was used to prepare the IrO_2-ATO catalysts. The physical and electrochemical characterisation of the catalysts were carried out using X-ray diffraction (XRD), scanning electron microscopy (SEM), transmission electron microscopy (TEM), powder conductivity, cyclic voltammetry (CV) and membrane electrode assembly (MEA) polarisation. The BET surface area and electronic conductivity of the supported catalysts were found to be predominantly arisen from the IrO_2. Supported catalyst showed higher active surface area than the pristine IrO_2 in CV analysis with 85% H_3PO_4 as electrolyte. The MEA performance using Nafion®−115 membrane at 80 °C and atmospheric pressure showed a better performance for IrO_2 loading $\geq$60 wt.% than the pristine IrO_2 with a normalised current density of 1625 mA cm^{-2} @1.8 V for the 60% IrO_2-ATO compared to 1341 mA cm^{-2} for the pristine IrO_2 under the same condition. The higher performance of the supported catalysts was mainly attributed to better dispersion of active IrO_2 on electrochemically inactive ATO support material, forming smaller IrO_2 crystallites. A 40 wt.% reduction in the IrO_2 was achieved by utilising the support material.

1. Introduction

Hydrogen is proposed to play an important role in the future energy scenario to form a sustainable energy carrier [1–3]. However current H_2 productions are mainly dominated by reforming of natural gas or other fossil fuels and are associated with greenhouse gas emissions [2], leading to atmospheric pollution and global warming. Electrolysis of water on the other hand is one of the most green and sustainable ways of hydrogen production when electricity from renewable energy such as wind, solar and tidal energy is being used. Proton exchange membrane water electrolyser (PEMWE) is the most attractive and efficient technology for the production of hydrogen from water. It is a sister technology to proton exchange membrane fuel cell and is based on similar design principle. PEMWE has several advantages compared to conventional alkaline electrolyser such as ecological cleanness, higher production rate, smaller mass to volume ratio, high power density, low power cost, high gas purity and high level

* Corresponding author. School of Chemical Engineering and Advanced Materials, Newcastle University, NE1 7RU, United Kingdom. Tel.: +44 (0) 191 222 5207; fax: +44 (0) 191 2225292.
E-mail addresses: v.puthiyapura@qub.ac.uk, v.k.puthiyapura@ncl.ac.uk, vinuchalaksd@gmail.com (V.K. Puthiyapura).

of safety [4]. However current PEMWE technology has drawbacks such as high material cost (PEM, catalyst and bipolar plates) and high over potential for the oxygen evolution reaction (OER) [5].

IrO_2 and RuO_2 are the most active electrocatalyst for the OER in PEMWE [6,7], but the stability of RuO_2 at high anodic potential is poor [7]. IrO_2 on the other hand has very good stability and gives high activity for the OER. However IrO_2 is approximately 2–3 times more expensive than RuO_2. Reducing the catalyst loading and subsequently reducing the cost is an important step towards commercialisation of PEMWE. Various methods have been adopted to reduce the precious metal loading on the electrode, such as adding non-precious element to form an alloy/bimetallic mixture or supporting the active catalyst on cheap and conductive high surface area support material [8,9]. Support material helps to increase the dispersion and reduce the agglomeration of the active catalyst. High surface area carbon is typically used as catalyst support in fuel cell. But the high corrosion rate (Equation (1)) of carbon at potentials where OER occurs restricts its use in the PEMWE anode [10,11].

$$C + 2H_2O \rightarrow CO_2 + 4H^+ + 4e^- \ (0.207 \ V \ vs. \ SHE, \ 25°C) \quad (1)$$
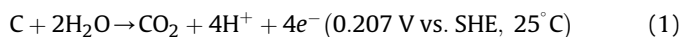
The standard electrode potential of the reaction (1) is 0.207 V vs. SHE at 25 °C [12] and carbon is thermodynamically unstable above this potential. Severe oxidation occurs only at higher potential above 0.9 V in the presence of water [10,11]. Due to the high oxidation potential at the electrolyser anode up to +2 V vs. SHE, the materials that can be used as supports are limited.

Ma et al. [9] studied TiC supported Ir as OER catalyst. Higher performance on 20 wt.% Ir/TiC compared to Ir black was obtained in cyclic voltammetry studies in 0.5 M H_2SO_4 solution [9]. An increase in MEA performance (Nafion®-112 membrane) with respect to the Ir loading in Ir/TiC from 10 wt.% to 40 wt.% was found in the MEA polarisation study [13] with a current density of 1002 mA cm^{-2} at potential of 1.8 V (80 °C, atmospheric pressure, Nafion®-112) for 40 wt.% Ir/TiC [13]. A higher stability was also observed for supported Ir/TiC catalyst compared to pristine Ir [14]. However it was reported that corrosion of TiC occur at anodic potential >0.8 V (vs. SHE) forming Ti^{4+}, CO and CO_2 [15–18]. At a potential of ~1.05 V vs. SHE, passivation occurs due to a TiO_2 layer formation and severe corrosion is observed at potential >1.75 V vs. SHE [18]. The non-conducting TiO_2 layer formation will reduce the conductivity and performance of the catalyst during long term operation. Other carbide such as Si–SiC [19] and TaC [20] were also studied as support material for electrolyser anode catalysts. IrO_2 supported TaC, prepared by the Adams method, was found to form a sodium–tantalum complex during the synthesis stage [20]. Even though TaC have good electronic conductivity (118 S cm^{-1}), this decreased by 10 orders of magnitude after the synthesis. TaC also has a low BET surface area (2.4 m^2 g^{-1}) [20]. Si–SiC support have good corrosion resistance, but suffer from poor electronic conductivity (1.8 × 10^{-5} S cm^{-1}) and low surface area (6 m^2 g^{-1}) [19].

Ti_4O_7, known as Ebonex, the major component in the homologous series of titanium sub oxides with general formula Ti_nO_{2n-1} ($4 \leq n \leq 10$), has a conductivity of about 1000 S cm^{-1} [12]. Ti_4O_7 has been used as a support material for the oxygen reduction reaction (ORR) and OER catalysts [21]. But on long term polarisation at high anodic potentials, a non-conductive TiO_2 layer was formed on this material limiting its use [22].

SnO_2, though is a poor electron conductor, doping with Sb(V), In(III) or F$^-$ increases its conductivity [23–25]. About 20 at% Sb can be added to SnO_2 to improve the conductivity of SnO_2 [25]. Antimony doped tin oxide (ATO) is widely used as an electronic conducting coatings, gas sensors, solar battery transparent electrodes [26,27]. ATO is stable in acidic media [28]. A bimetallic IrO_2–RuO_2

supported on commercial ATO nanoparticle with various loading (5, 10 and 20 wt.%) were studied by Marshall et al. [29]. CV studies in 0.5 M H_2SO_4 showed high activity for 20 wt.% $Ru_{0.25}Ir_{0.75}O_2$ on ATO. The OER performance decreased with decrease in catalyst loading and Ru content in the bimetallic oxide [29]. Wu et al. [30] studied ATO as support for RuO_2 catalyst. The RuO_2 particle size was ca. 10–15 nm while the ATO support had a particle size ca.30–40 nm for 20 wt.% RuO_2/ATO. A higher voltammetric charge was obtained for supported RuO_2 compared to pristine RuO_2 in half-cell studies with 0.5 M H_2SO_4 [30].

High stability of Pt supported on ATO in 85% phosphoric acid was reported by Tseung et al. [31]. Pristine Pt and ATO supported Pt (~10 wt.% Pt) were potentiostatically held at +700 mV vs. DHE in 85% H_3PO_4 at 150 °C for 720 h. It was found that the pristine Pt lost 63% of initial surface area, whereas ATO supported Pt lost only 25% of its initial surface area [31]. The performance of ATO supported Pt after the stability test was also higher than that of pristine Pt [31]. This was attributed to the lower agglomeration of the Pt crystallites on the ATO [31]. A higher stability of Pt/ATO as ORR catalyst was also reported by Yin et al. [32].
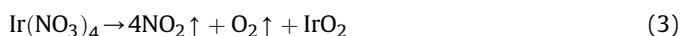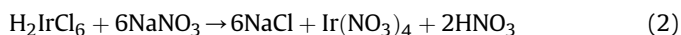
The objective of this study was to systematically investigate the effect of various parameters such as particle size, electronic conductivity and surface area on the performance of the ATO supported IrO_2 catalyst. ATO was selected due to its good electronic conductivity, thermal stability, commercial availability, high surface area and good electrochemical stability at anodic potentials [33].

2. Experimental

Commercially available ATO nanoparticle, Nanotek, 99.5% (Sb_2O_5:SnO_2 10:90 wt.%) from Alfa aesar (particle size of 22–44 nm, BET surface area 20–40 m^2 g^{-1}) was used as support. $H_2IrCl_6.xH_2O$ (Alfa aesar), $NaNO_3$ (Sigma Aldrich) were used as Ir precursor and oxidizing agent respectively.

2.1. Catalyst preparation

Supported IrO_2 catalyst was prepared by the modified Adams fusion method. H_2IrCl_6 solution was prepared in isopropanol (0.01 M). The ATO support was well dispersed in isopropanol to which the H_2IrCl_6 solution was added drop wise according to the stoichiometry to obtain the required IrO_2 loading (weight %) on the support. The solution was stirred well for 3 h, then excess $NaNO_3$ more than required by the stoichiometry (~50 g of $NaNO_3$ for 1 g of precursor) was added and stirred overnight [34]. The solvent was evaporated slowly and the obtained mixture was dried well and calcined at 500 °C for 1 h in a muffle furnace. The reaction occurred in Adams method is given by Equations (2) and (3) [8]. The NaCl formed was removed from the catalyst by washing with copious amount of DI water. Finally, the catalyst was dried in an air oven at ~70 °C overnight. The IrO_2 loading on the support was confirmed by EDX analysis.

$$H_2IrCl_6 + 6NaNO_3 \rightarrow 6NaCl + Ir(NO_3)_4 + 2HNO_3 \quad (2)$$

$$Ir(NO_3)_4 \rightarrow 4NO_2\uparrow + O_2\uparrow + IrO_2 \quad (3)$$

2.2. Physical characterisation

The X-ray diffraction (XRD) analysis was carried out using a PANalytical X'Pert Pro MPD (powered by a Philips PW3040/60 X-ray generator and fitted with an X'celerator) with Cu-Kα radiation ($\lambda = 1.541874$Å). The data were collected over a range of 5-100° 2θ

with a step size of 0.0334° and nominal time per step of 200 s. All scans were carried out in 'continuous' mode using the X'Celerator RTMS detector. Phase identification was carried out by means of the X'pert accompanying software program PANalytical High score plus in conjunction with the ICDD powder diffraction file 2 database (1999) and the crystallography open database (www. crystallography.net).

Scanning electron microscopy (SEM) and Energy dispersive X-ray (EDX) analyses were carried out in Fei X130 Esem-Feg (Environmental Electron Microscope-Field Emission Gun) at 20 kV for elemental analysis on uncoated samples in low vacuum mode and at 10 kV on gold coated samples in high vacuum mode for the images. The thermogravimetry analysis (TGA) was carried out using TGAQ500V20.10 Build 36 in air with temperature ramp from 30 °C to 900 °C at a rate of 10 °C min^{-1}. TEM analysis was carried out in Philips CM100 operated at 100 kV. The XPS analyses of the supported catalysts were carried in a K-alpha (Thermo scientific) instrument with micro focused monochromatic Al–K alpha source. The spectra were analysed using Casaxps software (version 2.3.16). The curve fitting was carried out using Gaussian–Lorentzian type profiles and the C 1s peak (284 eV) was used for the calibration of the peaks.

Electrical conductivity of the powder sample was calculated by measuring the resistance of the sample on measuring the current while applying voltage. The powder sample was pressed between two copper pistons placed in a standard micrometre. The resistance was measured at various thicknesses. A plot of thickness vs. resistance gives a linear relation and its gradient gives the resistivity (ρ) and thus the conductivity.

2.3. Electrochemical characterisation

The electrochemical characterisation was carried out in a three electrode cell using a voltalab PGZ50 potentiostat. An in-house built tantalum disk (geometric area of 0.1256 cm^2) encapsulated in teflon was used as working electrode. A Ag/AgCl (sat.KCl) and a Pt wire were used as reference and counter electrode respectively. The catalyst ink was prepared in isopropanol: water (3:2) solvent with Nafion® binder content of 20 wt.%. The ink was dispersed well in an ultra-sonicate bath for half an hour before drop casting 10 μl on the tantalum working electrode. The total catalyst (IrO$_2$ + ATO) loading on the working electrode was ~500 μg cm^{-2}. N$_2$ was passed through the electrolyte for 15 min before carrying out the test. Cyclic voltammetry (CV) were carried out at a potential between +0 and +1.25 V vs. Ag/AgCl at room temperature. A precondition of the electrode was carried out between these potentials for 10 cycles at 100 mV s^{-1}. CVs at different scan rate were recorded starting from 200 mV s^{-1} to 5 mV s^{-1}. Current values were normalised to the total catalyst weight on the electrode.

Membrane electrode assemblies (MEA) with the prepared catalysts as anode were prepared using a Nafion® −115 membrane by the catalyst coated membrane (CCM) method. Catalyst ink was prepared with catalyst, Nafion® solution and ethanol solvent and sprayed directly on the membrane using spray gun (Badger 100LG, USA). Pt/C (20 wt.%) from Alfa aesar was used as the cathode catalyst. Nafion® content on both electrodes were maintained at 15 wt.%. Nafion® membrane was pre-treated with 3%H$_2$O$_2$, 0.5 M H$_2$SO$_4$ and DI water successively before use. The cell body was made from titanium (10 × 10 × 3 cm) with a gold coated 1 cm^2 parallel flow field area. A gold coated Ti mesh and carbon paper (Torray) was used as current collectors for the anode and the cathode respectively. The anode and cathode catalyst loadings were 2 mg cm^{-2} and 0.5 mgPt cm^{-2} respectively. The prepared MEA was sandwiched between the current collectors and

assembled in the cell body using four M6 screws with a torque of 2 Nm.

DI water was pumped using a peristaltic pump to the anode side of the cell which was pre-heated to the required temperature by heating rods and controller. The cathode was kept dry. All measurements were carried out at atmospheric pressure. The potential difference was applied between the anode and cathode and the resulting current was measured using a power source (Thurlsby Thandar Instruments, PL3320).

3. Result and discussion

3.1. Thermal stability

The thermal stability of the support materials were studied using TGA analysis. The TGA of some of the commercially available materials such as titanium carbide (TiC) (Alfa aesar, 30–50 nm APS powder), titanium nitride (TiN) (Sigma Aldrich, <3 μm), tungsten carbide (WC) (Sigma Aldrich, powder, 2 μm, 99%), indium tin oxide (ITO) (Alfa aesar, 17–28 nm) and ATO nanoparticle (Alfa aesar, 22–44 nm) are given in Fig. 1. The TiC did not show any significant weight loss below 330 °C. A significant weight gain (25%) obtained from 330 °C to 650 °C indicated oxidation of TiC, forming TiO$_2$ and CO$_2$. TiN on the other hand showed a much higher thermal stability up to 400 °C. WC showed a thermal stability up to 500 °C with an onset of oxidation >500 °C. Even though the bulk oxidation occurred at the mentioned onset temperature for all samples, a surface oxidation will occur even at lower temperatures. The TiO$_2$ surface layer formed as a result of the oxidation of titanium based compounds will reduce the conductivity of the catalyst. ITO and ATO showed excellent thermal stability up to 800 °C with no significant weight gain/loss.

3.2. Structure and morphology

The XRD spectra of the ATO supported IrO$_2$ catalysts with various loading are given in Fig. 2. The ATO showed the characteristic peaks of SnO$_2$ (JCPDS-041-1445) at 26.6°, 33.9°, 37.9° and 51.8°. No peaks of Sb$_2$O$_5$ were observed in ATO, probably due to the entrance of Sb into the SnO$_2$ (90 wt.%) lattice [32]. The IrO$_2$ showed a rutile structure with characteristic peak at 28.02°, 34.73° and 54.10° (JCPDS-015-0876). The peaks of ATO were sharp and narrow compared to IrO$_2$, indicating a larger crystallite size.

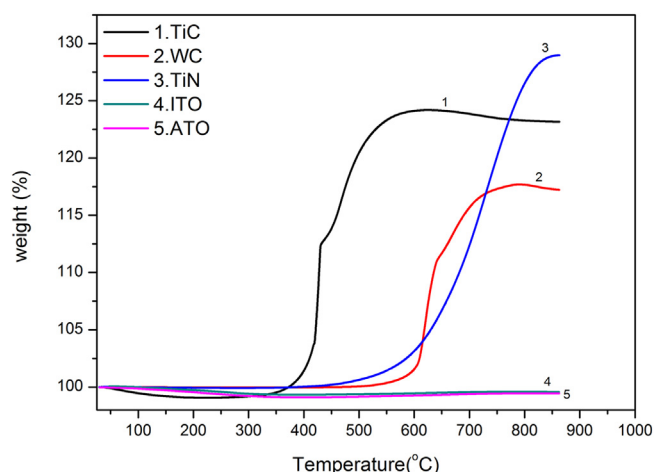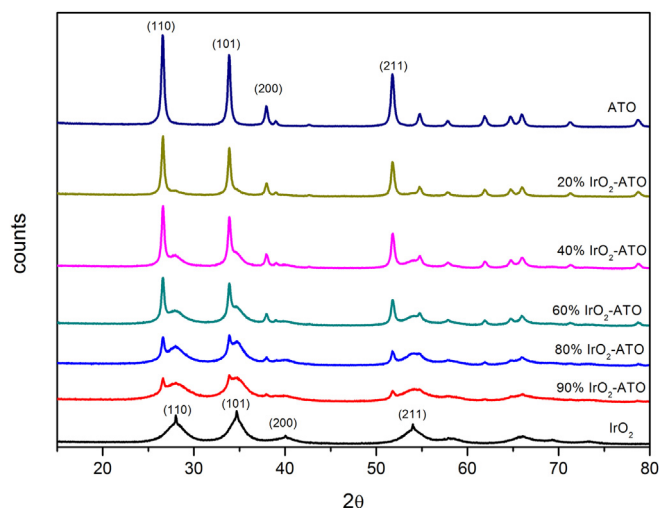**Fig. 1.** The TGA curve of some of the common support materials.

Fig. 2. XRD of IrO₂-ATO at different IrO₂ loading.

Fig. 3. Representative example of the peak fitting of the XRD peak (60% IrO₂-ATO).

The intensity of the IrO_2 peaks disappeared gradually and the SnO_2 peaks became prominent with the increase of the ATO wt.%. Two separate peaks for SnO_2 and IrO_2 were clear but were closely positioned. No shifts in the IrO_2 and SnO_2 peak position with respect to the composition were observed. This indicates that IrO_2 and ATO were present as separate phase and a single phase solid solution between the IrO_2 and SnO_2 was not formed. SnO_2 has a rutile structure similar to IrO_2 and the ionic radii of Ir^{4+} (0.077 nm) is close to that of Sn^{4+} (0.083 nm) [8]. According to Hume-Rothery theory, a solid solution/metal stable solution formation between the two oxides is possible [8,35]. However in our system, since pristine ATO was added to the Ir precursor for the synthesis of supported catalyst, an atomic level interaction between the two compounds leading to a solid solution is unlikely. Marshall et al. [36] reported that a solid solution between IrO_2 and SnO_2 is not favourable as it reduces the catalyst performance due to the increased ohmic resistance as well as change in the rate determining step at high current density.

Since the IrO_2 and SnO_2 peaks were closely positioned, a peak fitting was adapted to de-convolute the peaks for all the supported catalysts (Fig. 3). The crystallite size (t) was calculated using Scherrer equation (Equation (4)) from the de-convoluted peaks.

$$t = \frac{0.9\lambda}{\beta cos\theta} \qquad (4)$$

where t is the crystallite size, λ is the wavelength of the X-ray, β is the full width at half maximum and θ is the position of the peak. The average crystallite sizes of IrO_2 and ATO were calculated from the peaks at 28° and 34.7° and are given in Table 1. All supported catalyst showed a lower average crystallite size for IrO_2 compared to the pristine IrO_2 (Fig. 4) indicating that the support affects the crystallisation of IrO_2. The average crystallite size of ATO (calculated from the peaks at 26.6° and 33.9°) did not change significantly with composition with values around 22–24 nm (Fig. 4). The lower crystallite size of IrO_2 on the support can be attributed to a better Ir precursor dispersion on the support, leading to smaller crystallite formation. The pristine IrO_2 showed an average crystallite size of 6 nm which decreased with decrease in IrO_2 loading up to 60% IrO_2-ATO and starts increasing on reducing the IrO_2 loading further (Fig. 4). A similar trend was observed by Polonský et al. [20] for IrO_2/TaC catalysts. The lowest IrO_2 crystallite size was obtained for 90% IrO_2-ATO (3.8 nm). A decreasing in crystallite size for
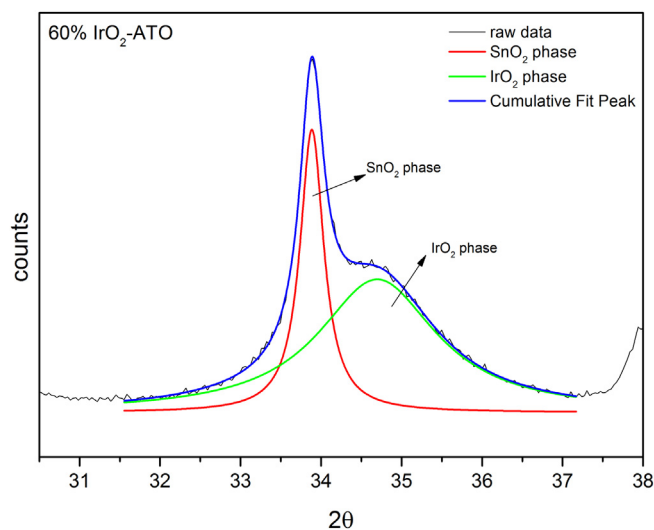
$Ir_xSn_{1-x}O_2$ catalyst prepared by Adams method were reported elsewhere [8]. The increase in crystallite size at lower IrO_2 loading may be explained based on the nucleation sites available for the crystallite formation. Pure IrO_2 is formed as a homogenous phase where it has to cross a significant energy barrier for the formation of the first IrO_2 nucleation site, whereas a supported catalyst is a heterogeneous system whereby the IrO_2 nucleation sites are formed on the support. The energy barrier in the latter case is lower than the former. Once a nucleation centre is formed, it is energetically favourable for IrO_2 to grow on it. At lower IrO_2 loading, the first nucleation centre is formed easily due to the lower activation energy and subsequently IrO_2 grows on it leading to a larger particle size [20].

The SEM and TEM of the 90% IrO_2-ATO and 40% IrO_2-ATO catalyst are given in Fig. 5. It was difficult to distinguish between the ATO and the IrO_2 particles from the SEM and TEM images. A very uniform morphology with similar particles can be seen in the SEM. Particle sizes in the range of 3–6 nm can be seen from the TEM for 90% IrO_2-ATO, whereas particles with two different sizes were observed for 40% IrO_2-ATO (Fig. 5). Even though it is difficult to clearly distinguish between two IrO_2 and ATO particles in TEM, a higher number of larger particles are evident for 40% IrO_2-ATO. This can be attributed to the large ATO nanoparticles. The XRD analysis gave a crystallite size of 23.2 nm for ATO in 40% IrO_2-ATO (Fig. 4). Since the BET surface area of ATO is lower than the pristine IrO_2, it is also possible that at higher IrO_2 loading, some of the IrO_2 exist as unsupported particles.

Table 1
Physical properties of the ATO supported IrO_2 catalysts.

| IrO₂ loading (wt.%)	Conductivity (S cm⁻¹)	Average t of IrO₂ (nm)	BET surface area (m² g⁻¹)	BET surface area normalised to IrO₂ loading (m² g⁻¹)	Particle size calculated from the BET surface area (nm)
100	4.9	6	112.8	112.8	4.6
90	4.8	3.8	126.5	137.2	3.8
80	4.1	4.1	109.3	129.1	4.0
60	1.4	4.1	86.9	124.8	4.1
40	2.0 × 10⁻¹	5.3	63.8	76.3	6.8
20	8.6 × 10⁻³	5.9	47.5	79.4	6.5
0	4.3 × 10⁻³	23.2[b]	20–40[a]		22.1–44

[a] Data from the supplier.
[b] Crystallite size of SnO₂.
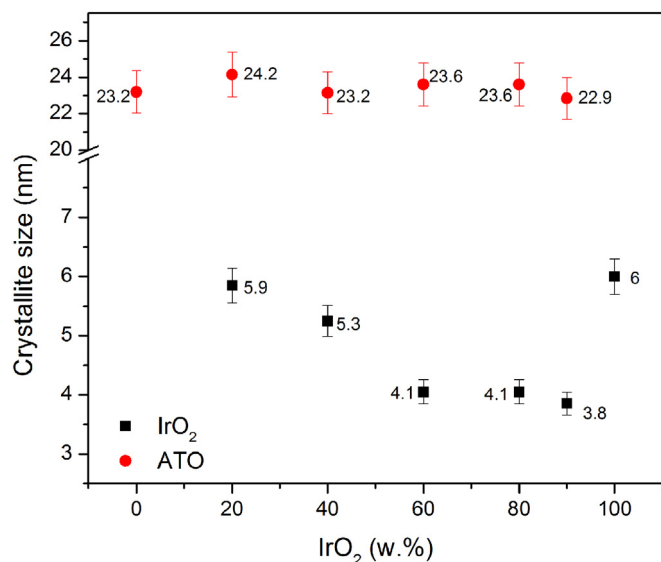
Fig. 4. The average crystallite size of IrO_2 and ATO in IrO_2-ATO calculated from the XRD using the Scherrer equation.

Table 2
Ir composition of IrO_2-ATO catalyst from the EDX analysis.

Catalyst	Ir wt.% obtained from EDX analysis	Desired Ir wt.%
20% IrO_2-ATO	17.9	17.2
40% IrO_2-ATO	33.6	34.3
60% IrO_2-ATO	50.3	51.4
80% IrO_2-ATO	71.2	68.6
90% IrO_2-ATO	76.2	77.2

The Ir wt.% for the supported catalyst obtained from the EDX analysis is given in Table 2. The loading is almost the same as that of the precursor used and indicates that there was no significant material loss during the synthesis and washing stage. No compounds other than ATO and IrO_2 were found in the XRD or the EDX analysis and it can be concluded that no side reaction occurred between ATO and $NaNO_3$ [37].

3.3. Powder conductivity

A linear relationship between the thicknesses vs. resistance (Fig. 6 inset) was obtained for the catalyst powder samples measured at room temperature. The electrical conductivity was calculated from the slope of the linear plot of thickness vs. resistance and is given in Table 2 and Fig. 6. The conductivity of the pristine IrO_2 (4.9 S cm^{-1}) was 3 orders of magnitude higher than that of the ATO support (4.3×10^{-3} S cm^{-1}). A conductivity of the same order of magnitude for IrO_2 was reported elsewhere [8]. The conductivity of the supported catalyst decreased with decrease in IrO_2 loading (Fig. 6) indicating that the conductivity was predominantly contributed by the IrO_2. Even though the support itself has low conductivity, addition of IrO_2 significantly increased the conductivity of the supported catalyst particles. A 60% IrO_2 loading increased the conductivity by three order of magnitude compared
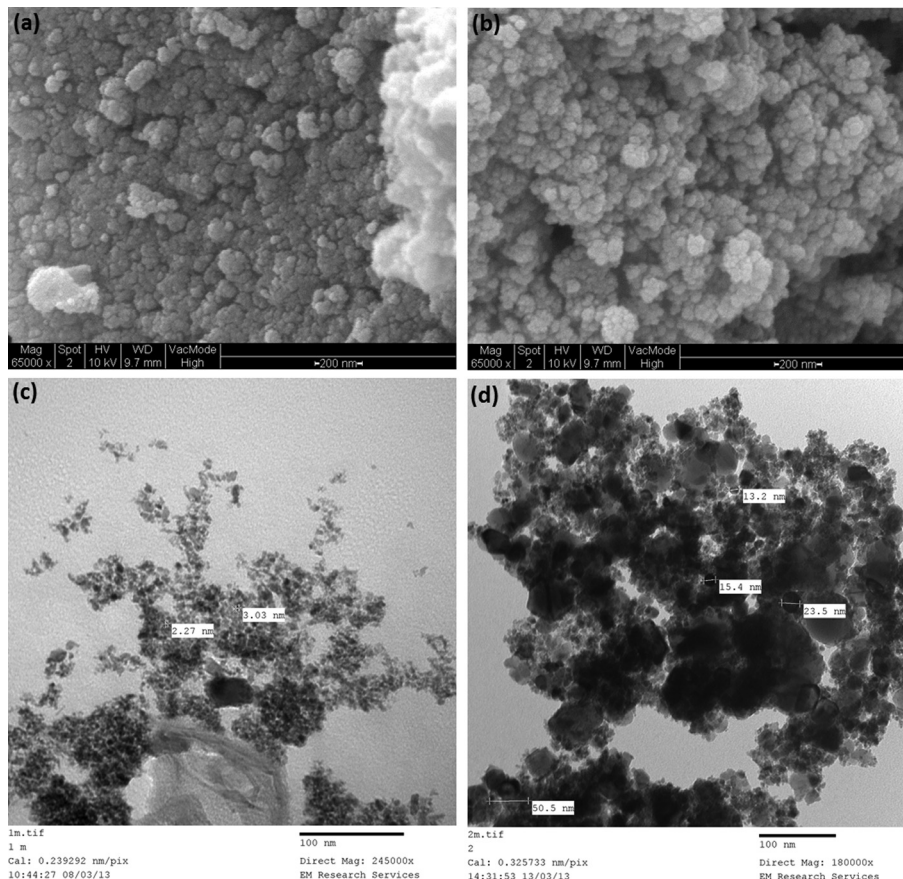

Fig. 5. SEM and TEM image of (a), (c) 90% IrO_2-ATO (b), (d) 40% IrO_2-ATO respectively.
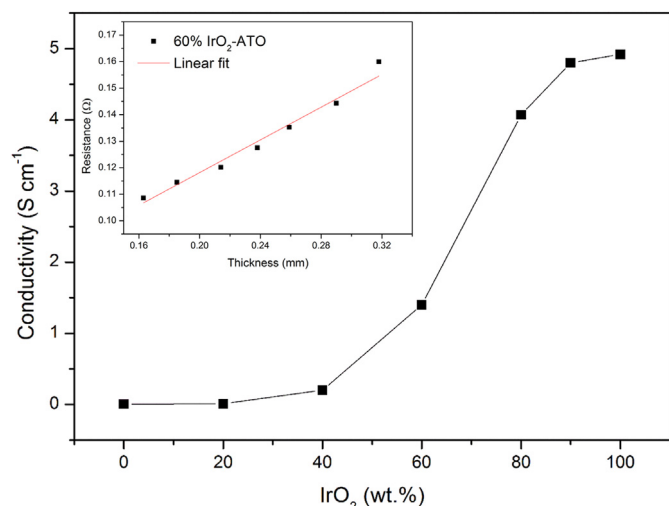
Fig. 6. The conductivity of IrO$_2$-ATO catalyst with respect to the IrO$_2$ loading. Inset shows the linear relation between the thicknesses vs. resistance of 60% IrO$_2$-ATO.

Fig. 7. Linear trend in the BET surface area of IrO$_2$-ATO catalyst with respect to composition.

to the ATO support. An increase in conductivity by five order of magnitude was reported elsewhere for 60% Pt/TiO$_2$ compared to TiO$_2$ support [38]. The resistivity of oxides suggested to be mainly comes from the inter-grain region and the conduction occur mainly by a 'hopping mechanism' between the grains [8]. Thus, the conductivity depends on various factors such as the conductivity of individual particles, contact between the particles, their packing and applied pressure [39]. Compared to dimensionally stable anode (DSA) type electrode, where the catalyst oxide film is formed on a metal support such as titanium, powder catalyst system will have higher resistivity due to higher number of grain regions [40]. Lodi et al. [40] reported that, DSA electrode with cracked morphology of RuO$_2$ have two orders of magnitude higher resistivity compared to compact RuO$_2$ due to the breakdown of conduction path in the cracked morphology. The conductivity of the supported IrO$_2$ for loadings up to 60% IrO$_2$-ATO was of the same order of magnitude to that of the pristine IrO$_2$ and decreased by one order of magnitude from 60% IrO$_2$-ATO to 40% IrO$_2$-ATO (Table 2). The large conductivity at higher loading was due to the higher IrO$_2$ amount as well as the full coverage of ATO surface by conductive IrO$_2$. Since conductivity of ATO was 3 orders of magnitude lower than pristine IrO$_2$, a partial coverage of ATO can lead to a poor conduction network. The loss of catalyst conductivity can contribute to the performance loss of the MEA in PEMWE due to the subsequent increase in the full cell resistance [8,41].

Based on the catalyst layer thickness of 5–10 μm and acceptable ohmic drop on the anode of 10 mV, Marshall et al. [8] proposed a resistivity value of $\leq$10 Ω cm^{-1} as suitable for the anode catalyst in PEMWE. According to this, a loading of $\geq$40% IrO$_2$-ATO can be considered as suitable anode catalyst in PEMWE based on their conductivity. However, resistivity of the membrane and ionomer in the catalyst layer needs to be considered in real electrolyser operation. Also the porous nature of the current collector will increase the lateral resistivity further increasing the ohmic loss [34].

3.4. BET surface area

The BET surface areas of the supported catalysts are given in Table 2. The BET surface area of the pristine IrO$_2$ (112.7 m^2 g^{-1}) was approximately 3 times higher than the ATO support (20–40 m^2 g^{-1}). The surface area varies linearly with the IrO$_2$

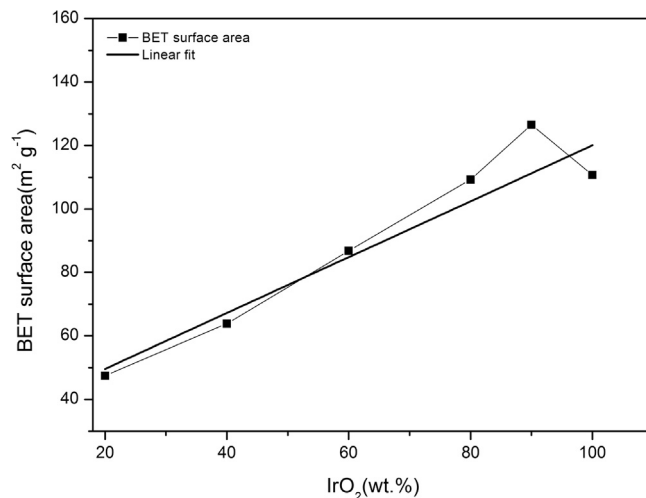loading (Fig. 7) indicating that, the surface area was mainly contributed by the IrO$_2$ with insignificant contribution from the support. A BET surface area of 121 m^2 g^{-1} was reported elsewhere for IrO$_2$ prepared by the Adams method [19,20]. A higher surface area for 90% IrO$_2$-ATO than the pristine IrO$_2$ indicates that the active component was well dispersed on the support forming small particles. The support material acts as nuclei for the dispersion and oxidation of IrO$_2$ intermediate during the synthesis. Even though a higher surface area of the support material is generally prescribed; it is advantageous only when the support has a higher or similar conductivity to that of the active component. A higher surface area support with poor conductivity will decrease the performance due to the overall decrease in conductivity of the catalyst layer.

The BET surface area normalised to IrO$_2$ loading (excluding the support surface area) is also given in Table 2. Considering the IrO$_2$ as a sphere with diameter ('t' m) and density ρ (11.6 g cm^{-3}) having specific surface area SSA (m^2 g^{-1}), the particle size (t) can be calculated using the Equation (5),

$$t = \frac{6}{SSA \times \rho} \tag{5}$$

The obtained particle size from the BET surface area is given in Table 2. The particle size calculated is similar to that calculated from the XRD, indicating a good dispersion of the IrO$_2$ on the support.

3.5. XPS analysis

The survey spectra from 400 eV to 600 eV of various prepared supported catalysts are compared in Fig. 8. The peaks of Sb 3d$_{5/2}$ and O1s (530.1 eV) as well as Sn 3d$_{3/2}$ and Ir 4p$_{3/2}$ (496.2 eV) overlap each other. The distinguishable peaks of Ir are Ir 4d$_{3/2}$ (~313.65), Ir 4d$_{5/2}$ (~298.1 eV) and Ir 4f peaks. For Sn, it is Sn 3d$_{5/2}$ (~487.19 eV). A gradual decrease in the Sb 3d$_{3/2}$ and Sn 3d$_{5/2}$ peaks can be seen in Fig. 8 with an increase in IrO$_2$ loading indicating coverage of the ATO surface by the IrO$_2$. This is consistent with XRD (Fig. 2) whereby a similar increase in the intensity of SnO$_2$ peaks was observed with a decrease in IrO$_2$ loading.

The Ir 4f scan of 90% IrO$_2$-ATO is given in Fig. 9. A similar peak fitting was reported elsewhere [8,42]. The two pairs of peaks indicate the Ir is present in more than one valence state [8]. The 5th peak located at ~67.6 eV has been suggested to be due to the final state screening [42]. The binding energy (BE) for Ir 4f$_{5/2}$ (64.8 eV)
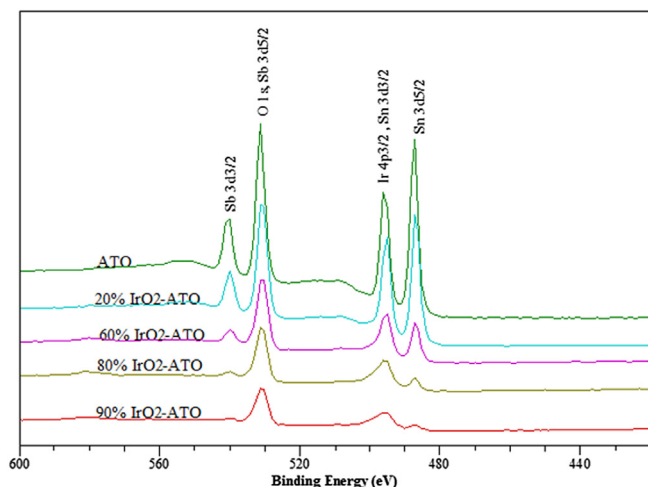
Fig. 8. The XPS survey spectra of various IrO$_2$-ATO catalysts.

Fig. 10. CV of IrO$_2$ at different scan rate in 85% H$_3$PO$_4$ at room temperature. The inset shows the linear relation between the current (~0.75 V) vs. scan rate.

and Ir 4f$_{7/2}$ (61.9 eV) were higher than for the metallic Ir (60.9 eV for 4f$_{7/2}$ and 63.8 eV for 4f$_{5/2}$) and was assigned to Ir^{4+} chemical state in the literature [8,43–46]. The pair of peaks at ~63 eV and ~66.2 eV have higher BE than Ir^{4+} and may be attributed an existence of higher oxidation state of IrO$_2$ [44]. Slavcheva [45] assigned the lower BE peak pair (61.9 eV) to Ir^{3+} and the higher BE peak pair (~62.9 eV) to Ir^{4+}. Due to the considerable disagreement in the literature [42], it is not possible to conclude exactly which Ir species is present. However it is certain that all the Ir species were present as oxides and no metallic Ir was detected. The Sn 3d$_{5/2}$ peak at BE of 487.2 eV (484.6 eV for Sn 3d$_{5/2}$ in metallic Sn) represent SnO$_2$ stoichiometric state [43].

3.6. Electrochemical studies

The cyclic voltammogram (CV) of IrO$_2$ in 0.5 M H$_2$SO$_4$ is widely seen in the literature [7,47,48] with no distinguishable features. However it was reported elsewhere that IrO$_2$ redox peaks are clearer in 85% H$_3$PO$_4$ [19]. Also H$_3$PO$_4$ doped PBI are recently getting wide interest as replacement to Nafion$^®$ for high temperature operation of electrolyser. Thus 85% H$_3$PO$_4$ was used in this study as electrolyte to study the electrochemical behaviour of the supported
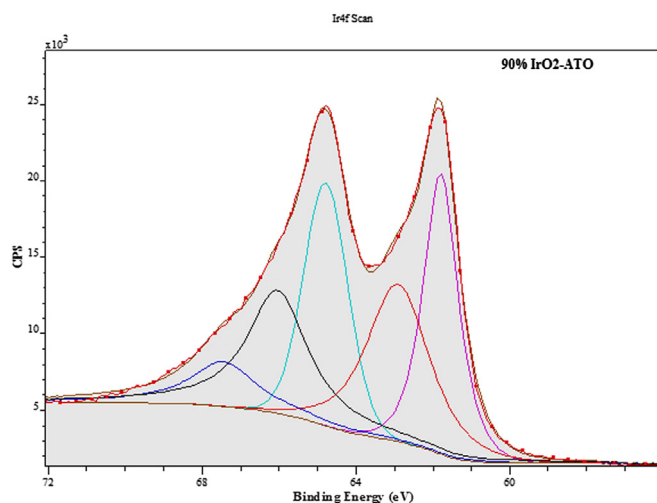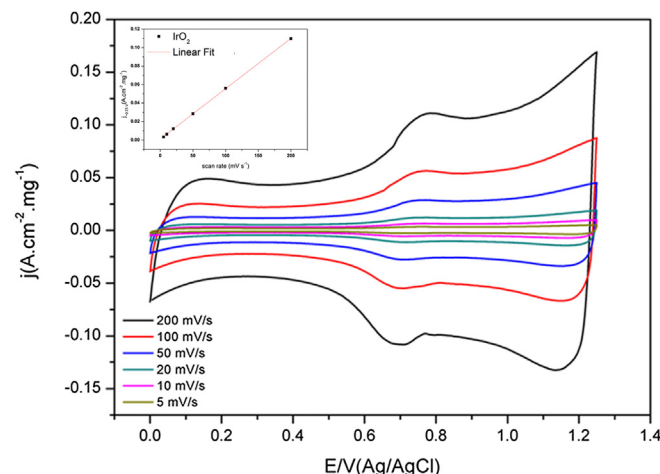
catalysts. The CV of IrO$_2$ in 85% H$_3$PO$_4$ is given in Fig. 10. The redox peaks of IrO$_2$ were clearly visible in 85% H$_3$PO$_4$ as reported in literature [19]. The CV showed characteristic shape of IrO$_2$ with narrow region at potential lower than +0.5 V and wider region above +0.5 V vs. Ag/AgCl indicating a high charge storage capacity of IrO$_2$ [49]. The pristine IrO$_2$ and supported IrO$_2$ gives characteristic peaks of IrO$_2$ at ~0.78 V and ~1 V (vs.Ag/AgCl) and is attributed to the redox transition of Ir(III)/Ir(IV) and Ir(IV)/Ir(VI) respectively. This is due to the surface redox reaction between IrO$_2$ and H$^+$ according to the Equation (6) [48,50–52]. The Ir(III)/Ir(IV) and Ir(IV)/Ir(VI) transition can be realised when $x = 1$, $y = 1$, $\delta = 1$ and $x = 1$, $y = 2$, $\delta = 2$ respectively. The capacitance behaviour in the IrO$_2$ comes from the pseudo-capacitance (due to the proton exchange reaction) and the double layer capacitance (due to the ion adsorption) [51]. The integration of the CV curve between the potential limit gives the voltammetric charge (q^*) and is a measure of the number of active sites available to exchange proton with the solution. i.e. electrochemical active surface area [53–55]. The q^* is often used in the literature to quantify the electrochemical active surface area of the noble metal oxides [47,53–58].
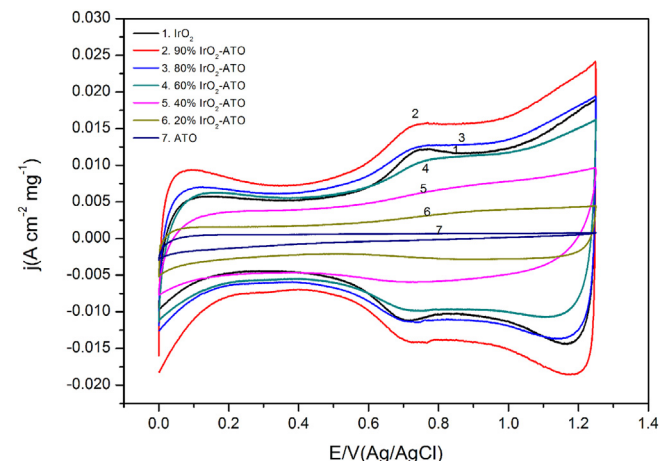
$$\text{IrO}_x(\text{OH})_y \leftrightharpoons \text{IrO}_{x+\delta}(\text{OH})_{y-\delta} + \delta\text{H}^+ + \delta e^- \tag{6}$$

Fig. 9. Typical Ir 4f scans of IrO$_2$-ATO catalysts.
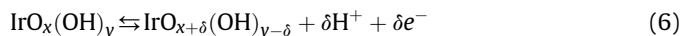

Fig. 11. CV of IrO$_2$-ATO with different IrO$_2$ composition in 85% H$_3$PO$_4$ at room temperature. Scan rate 20 mV s^{-1}.

Table 3
Voltammetric charge of IrO_2-ATO at room temperature in 85% H_3PO_4. Scan rate 20 mV s^{-1}.

Sample	Voltammetric charge (q^*) (mC cm^{-2} mg^{-1})	Voltammetric charge normalised to IrO_2 loading (q^*_{norm}) (mC cm^{-2} mg^{-1})
IrO_2	1700	1700
90% IrO_2-ATO	1990	2210
80% IrO_2-ATO	1840	2300
60% IrO_2-ATO	1570	2620
40% IrO_2-ATO	980	2450
20% IrO_2-ATO	493	2465
ATO	122	–

The CV of IrO_2-ATO catalyst recorded at 20 mV s^{-1} at room temperature with different IrO_2 loading in 85% H_3PO_4 is given in Fig. 11. The charging current response from the ATO at all potential was one order of magnitude lower than that from 20% IrO_2-ATO (Fig. 11), indicating that the current observed in IrO_2-ATO catalyst mainly comes from the IrO_2. The CVs of all catalysts were symmetrical with respect to the zero current axes independent of the scan rate (Figs. 10 and 11) suggesting a reversible reaction at the catalyst surface. The peak current for the Ir (III)/Ir(IV) transition around ~0.75 V was plotted against the scan rate and a linear plot was obtained Fig. 10 (inset) indicate that the proton insertion/ejection reaction was not influenced by diffusion [59—62].

The voltammetric charge obtained from the CV of various supported catalyst at 20 mV s^{-1} is given in Table 3. The 90% IrO_2-ATO (1990 mC cm^{-2} mg^{-1}) and 80% IrO_2-ATO (1840 mC cm^{-2} mg^{-1}) gave higher voltammetric charge compared to the pristine IrO_2 catalyst (1700 mC cm^{-2} mg^{-1}). The active area for the supported catalyst are in the order 90% IrO_2-ATO >80% IrO_2-ATO > IrO_2 >60% IrO_2-ATO >40% IrO_2-ATO >20% IrO_2-ATO > ATO. The higher active area for the 90% IrO_2-ATO and the 80% IrO_2-ATO are in agreement with the observation by Nikiforov et al. [19] where a higher active surface area for 90% IrO_2/Si—SiC in comparison to pristine IrO_2 was obtained in 85% H_3PO_4 and was attributed to smaller IrO_2 particles (~ 3 nm for 90% IrO_2/Si—SiC compared to 5.5 nm for pristine IrO_2) as well as better dispersion of IrO_2 on the support. It was clear from the BET surface area analysis, that 90% IrO_2-ATO have higher surface area than the pristine IrO_2, whereas the 80% IrO_2-ATO have comparable BET surface areas and conductivities to that of IrO_2

(Table 2). The voltammetric charge normalised to IrO_2 loading (q^*_{norm}) is also given in Table 3. The 60% IrO_2-ATO showed the highest q^*_{norm} (2620 mC cm^{-2} mg^{-1}) which is ~1.5 times higher than that of the pristine IrO_2 (q^*_{norm}=1700 mC cm^{-2} mg^{-1}). The higher q^*_{norm} of the supported catalysts (Table 3) indicates that the IrO_2 dispersion increases with increase in support addition [29]. This was supported by the XRD analysis whereby a lower IrO_2 crystallite sizes were observed for all the supported catalysts (Fig. 4). It may be assumed that an optimum balance between the IrO_2 particle size and conductivity was maintained for IrO_2 loading ≥60% IrO_2-ATO giving rise to higher voltammetric charge.

3.7. Electrolyser tests

The performance of the as prepared IrO_2 supported catalyst as anode was evaluated in an MEA prepared with Nafion® −115 membranes and Pt/C (20 wt.%) cathode catalyst at 80 °C and atmospheric pressure. The effect of temperature on the MEA performance was evaluated by testing the MEA at three different temperatures 25 °C, 50 °C and 80 °C. The polarisation plot of 80% IrO_2-ATO at various temperatures is given in Fig. 12. The current density at 1.8 V for 25 °C, 50 °C and 80 °C were 498, 728 and 1266 mA cm^{-2} respectively. The current density @1.8 V and 80 °C was ~2.5 times higher than that at 25 °C. The increased performance of the MEA with increase in temperature can be attributed to the faster electrode kinetics and increased Nafion® conductivity at higher temperature [63]. Thus 80 °C were used for the performance analysis of all the MEA's.

MEAs prepared with IrO_2-ATO with various IrO_2 loading at 80 °C are compared in Fig. 13 and Table 4. The pristine IrO_2 and 90% IrO_2-ATO gave the best performance among all the tested MEAs with a potential of 1.73 V at 1 A cm^{-2} which equates to a cell efficiency ($\varepsilon_{\Delta G}$) of 68% and energy consumption of 4.14 kWhr Nm^{-3} H_2 at 80 °C. The MEA performance decreased with a decrease in the IrO_2 loading. The cell potential increased from 1.74 V, 1.8 V−1.96 V @ 1A cm^{-2} for 80% IrO_2-ATO, 60% IrO_2-ATO and 40% IrO_2-ATO respectively. In order to eliminate the effect of different IrO_2 loading on the support, the current density @1.8 V is normalised to the IrO_2 loading (j_{norm}) and the normalised current density values are given in Table 4. The j_{norm} @1.8 V increased with a decrease in the IrO_2 loading up to 60% IrO_2-ATO and decreased with further decrease in the IrO_2 loading. The 60% IrO_2-ATO (1625 mA cm^{-2} @1.8 V) had a j_{norm} of about 1.2 times higher than the pristine IrO_2. This indicates
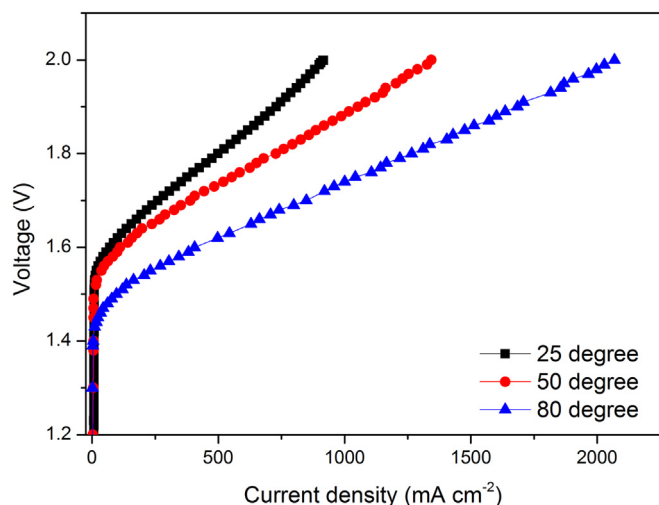
Fig. 12. The effect of temperature on performance of 80% IrO_2-ATO (Nafion® −115 membrane, Pt/C (20%) cathode catalyst.
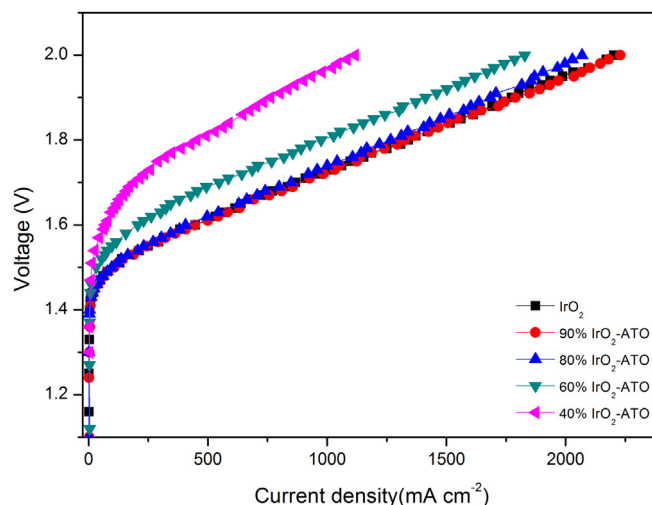
Fig. 13. MEA polarisation of IrO_2-ATO anode catalyst at 80 °C and ambient pressure. Nafion® −115 membrane, Pt/C (20 wt.%) cathode catalyst.

Table 4
MEA performance of IrO_2-ATO at various IrO_2 loading at 80 °C.

Anode catalyst	Current density @1.8 V (mA cm^{-2})	Current density@1.8 V normalised to IrO_2 weight (mA cm^{-2})	Cell voltage @1 A cm^{-2} (V)	Cell voltage @ 0.1 A cm^{-2} (V)
IrO_2	1341	1341	1.73	1.50
90% IrO_2	1327	1473	1.73	1.50
80% IrO_2	1266	1583	1.74	1.50
60% IrO_2	975	1625	1.80	1.55
40% IrO_2	453	1133	1.96	1.63

that the performance of the supported catalysts with up to 60 wt.% IrO_2 loading is better than that of the pristine IrO_2. This is a significant achievement in terms of the cost of the catalyst as 40 wt.% reduction in the active catalyst can be achieved using support material. Higher performance of the catalyst up to 60 wt.% IrO_2 loading on ATO can be attributed to their lower particle size, higher BET surface area and similar conductivity to that of pristine IrO_2. In our previous publication on supported IrO_2 catalyst, it was observed that the crystallite size of active catalyst on the support has significant influence in the MEA performance [64]. A 60% IrO_2–TiO_2 with IrO_2 crystallite size of 5 nm showed a cell voltage of 1.78 V@ 1 A cm^{-2} [64] which is comparable to the performance of 60% IrO_2-ATO (1.8 V@1 A cm^{-2}) obtained here. The better performance with TiO_2 support [64] compared to the ATO support here, is assumed to be due to the higher surface area associated with the support itself and the 60% IrO_2 loading on it. A gradual increase in the performance of the MEA with respect to increase in the active catalyst loading for Ir/TiC was reported elsewhere [13] and was attributed to the degree of coverage of poor conducting TiC and subsequent increase in conductivity. Here, up to 60% IrO_2-ATO, the electronic conductivity was of the same order of magnitude to that of the pristine IrO_2 and decreased by one order of magnitude for the 40% IrO_2-ATO. This might be due to the lower particle size and better dispersion of the active IrO_2 catalyst on the ATO support covering its surface for IrO_2 loading >60 wt.% as explained in Section 3.3. It was clear that the catalyst conductivity and IrO_2 particle size have significant influence in the performance of the MEA. The low performance for 40% IrO_2-ATO may be attributed to its lower IrO_2 content (thus lower available active sites), lower electrical conductivity (2×10^{-1} S cm^{-1}) and larger crystallite size (5.3 nm) compared to IrO_2 loading > 60 wt.% IrO_2 (Table 2). Based on these observations, 60% IrO_2-ATO can be considered as cut off loading for the ATO supported IrO_2 catalysts with a full IrO_2 coverage of the support.

The cell voltage at low current density of 100 mA cm^{-2} where ohmic resistance and bubble effect does not significantly influence the MEA performance is used to compare the activity of the anode catalyst. The cathode performance can be considered as equal for all the MEA especially at low current density due to the faster kinetics of HER on Pt electrode. A cell voltage of 1.5 V was observed for the pristine IrO_2, 90% IrO_2-ATO and 80% IrO_2 @0.1 A cm^{-2}. The higher performance obtained for 90% IrO_2-ATO and 80% IrO_2-ATO in the CV analysis was not observed in the MEA analysis which probably is due to the large ohmic resistance (catalyst layer, membrane and cell components) associated with MEA test. The 60% IrO_2-ATO showed only 50 mV (1.55 V @ 0.1 A cm^{-2}) higher voltage compared to the pristine IrO_2 (1.50 V @ 0.1 A cm^{-2}). The difference between the cell voltages @ 0.1 A cm^{-2} and 1 A cm^{-2} increased from 230 mV for 90% IrO_2-ATO to 330 mV for 40% IrO_2-ATO (Table 4) indicating a higher ohmic drop at lower IrO_2 loading. At higher current density mass transport and electrical/ionic conductivity will influence the MEA performance. It was also clear from the powder conductivity analysis that the conductivity decreased with decrease in the IrO_2 loading (Table 2).

Overall, considering the MEA performance and loading of the IrO_2 on the anode catalyst layer, a 60% IrO_2-ATO can be proposed as suitable catalyst for PEMWE with a of 40 wt.% reduction in the precious metal content.

4. Conclusion

ATO nanoparticles (22–44 nm) were used as a support material for IrO_2 in PEMWE anode. A modified Adams method was adapted for the synthesis of supported catalysts. The supported catalysts showed lower crystallite size compared to the pristine IrO_2. A gradual increase in the intensities of the SnO_2 peaks with decrease in IrO_2 loading was also clear from XRD and XPS analysis indicating coverage of the ATO support by IrO_2 with increase in IrO_2 loading. Both the powder conductivity and the BET surface area increased with increase in IrO_2 loading indicating that the conduction and the surface area were contributed primarily by IrO_2. The BET surface area of ATO (20–40 m^2 g^{-1}) was approximately 3 times lower than that of pristine IrO_2 (112.7 m^2 g^{-1}) whereas the conductivity of ATO (4.29×10^{-3} S cm^{-1}) was 3 orders of magnitude lower than that of pristine IrO_2 (4.92 S cm^{-1}). However a loading of $\geq$60% IrO_2-ATO gave a conductivity of the same order of magnitude to that of pristine IrO_2, indicating that the IrO_2 forms a continuous electronic network at $\geq$60% IrO_2-ATO loading, below which a significant decrease in conductivity was observed.

Electrochemical characterisation in 85% H_3PO_4 at room temperature showed characteristic peaks of IrO_2 and the 90% IrO_2-ATO and 80% IrO_2-ATO showed higher active surface than the pristine IrO_2. MEA analyses with Nafion®-115 membrane and the prepared catalyst as anode electrode were also in agreement with the CV analysis. IrO_2 loading $\geq$60% IrO_2-ATO showed better performance than that of the pristine IrO_2 after normalising the current density for IrO_2 loading. The increased performance can be attributed to the better dispersion of the IrO_2 on ATO resulting in smaller crystallites and large surface area. A reduction of 40 wt.% was achieved by utilising ATO support with better performance than the pristine IrO_2.

References

[1] J. Turner, G. Sverdrup, M.K. Mann, P.-C. Maness, B. Kroposki, M. Ghirardi, R.J. Evans, D. Blake, Int. J. Energy Res. 32 (2008) 379–407.
[2] K. Mazloomi, C. Gomes, Renew. Sustain. Energy Rev. 16 (2012) 3024–3033.
[3] M. Momirlan, T.N. Veziroglu, Renew. Sustain. Energy Rev. 6 (2002) 141–179.
[4] S.A. Grigoriev, V.I. Porembsky, V.N. Fateev, Int. J. Hydrogen Energy 31 (2006) 171–175.
[5] P.W.T. Lu, S. Srinivasan, J. Appl. Electrochem. 9 (1979) 269–283.
[6] T. Sergio, J. Electroanal. Chem. Interfacial Electrochem. 111 (1980) 125–131.
[7] S. Song, H. Zhang, X. Ma, Z. Shao, R.T. Baker, B. Yi, Int. J. Hydrogen Energy 33 (2008) 4955–4961.
[8] A. Marshall, B. Børresen, G. Hagen, M. Tsypkin, R. Tunold, Mater. Chem. Phys. 94 (2005) 226–232.
[9] L. Ma, S. Sui, Y. Zhai, J. Power Sources 177 (2008) 470–477.
[10] L.M. Roen, C.H. Paik, T.D. Jarvi, Electrochem. Solid-State Lett. 7 (2004) A19–A22.
[11] F. Maillard, A. Bonnefont, F. Micoud, Electrochem. Commun. 13 (2011) 1109–1111.
[12] H. Chhina, S. Campbell, O. Kesler, J. Power Sources 161 (2006) 893–900.

[13] S. Sui, L. Ma, Y. Zhai, Asia-Pacific J. Chem. Eng. 4 (2009) 8—11.
[14] L. Ma, S. Sui, Y. Zhai, Int. J. Hydrogen Energy 34 (2009) 678—684.
[15] A. Ignaszak, C. Song, W. Zhu, J. Zhang, A. Bauer, R. Baker, V. Neburchilov, S. Ye, S. Campbell, Electrochim. Acta 69 (2012) 397—405.
[16] H.O. Pierson. in: Noyes Publications, United States of America, 1996.
[17] R.D. Cowling, H.E. Hintermann, J. Electrochem. Soc. 118 (1971) 1912—1916.
[18] R.D. Cowling, H.E. Hintermann, J. Electrochem. Soc. 117 (1970) 1447—1449.
[19] A.V. Nikiforov, A.L. Tomás García, I.M. Petrushina, E. Christensen, N.J. Bjerrum, Int. J. Hydrogen Energy 36 (2011) 5797—5805.
[20] J. Polonský, I.M. Petrushina, E. Christensen, K. Bouzek, C.B. Prag, J.E.T. Andersen, N.J. Bjerrum, Int. J. Hydrogen Energy 37 (2012) 2173—2181.
[21] S. Siracusano, V. Baglio, C. D'Urso, V. Antonucci, A.S. Aricò, Electrochim. Acta 54 (2009) 6292—6299.
[22] G. Chen, S.R. Bare, T.E. Mallouk, J. Electrochem. Soc. 149 (2002) A1092—A1099.
[23] C. Goebbert, R. Nonninger, M.A. Aegerter, H. Schmidt, Thin Solid Films 351 (1999) 79—84.
[24] J. Zhang, L. Gao, Mater. Res. Bull. 39 (2004) 2249—2255.
[25] L. Shimin, D. Wanyu, G. Yousong, C. Weiping, Phys. Scr. 85 (2012) 065601.
[26] M. Zheng, B. Wang, Trans. Nonferrous Metals Soc. China 19 (2009) 404—409.
[27] T.J. Liu, Z.G. Jin, L.R. Feng, T. Wang, Appl. Surf. Sci. 254 (2008) 6547—6553.
[28] F. Vicent, E. Morallón, C. Quijada, J.L. Vázquez, A. Aldaz, F. Cases, J. Appl. Electrochem. 28 (1998) 607—612.
[29] A.T. Marshall, R.G. Haverkamp, Electrochim. Acta 55 (2010) 1978—1984.
[30] X. Wu, K. Scott, Int. J. Hydrogen Energy 36 (2011) 5806—5810.
[31] A.C.C. Tseung, S.C. Dhara, Electrochim. Acta 20 (1975) 681—683.
[32] M. Yin, J. Xu, Q. Li, J.O. Jensen, Y. Huang, L.N. Cleemann, N.J. Bjerrum, W. Xing, Appl. Catal. B Environ. 144 (2014) 112—120.
[33] G. Chen, X. Chen, P.L. Yue, J. Phys. Chem. B 106 (2002) 4364—4369.
[34] E. Rasten, G. Hagen, R. Tunold, Electrochim. Acta 48 (2003) 3945—3952.
[35] X. Chen, G. Chen, P.L. Yue, J. Phys. Chem. B 105 (2001) 4623—4628.
[36] A. Marshall, B. Børresen, G. Hagen, M. Tsypkin, R. Tunold, Electrochim. Acta 51 (2006) 3161—3167.
[37] V.K. Puthiyapura, S. Pasupathi, S. Basu, X. Wu, H. Su, N. Varagunapandiyan, B. Pollet, K. Scott, Int. J. Hydrogen Energy 38 (2013) 8605—8616.
[38] R.E. Fuentes, B.L. García, J.W. Weidner, J. Electrochem. Soc. 158 (2011) B461—B466.
[39] J. Sánchez-González, A. Macías-García, M.F. Alexandre-Franco, V. Gómez-Serrano, Carbon 43 (2005) 741—747.
[40] G. Lodi, C. de Asmundis, S. Ardizzone, E. Sivieri, S. Trasatti, Surf. Technol. 14 (1981) 335—343.
[41] A. Marshall, B. Bårresen, G. Hagen, M. Tsypkin, R. Tunold, Energy 32 (2007) 431—436.
[42] L. Atanasoska, R. Atanasoski, S. Trasatti, Vacuum 40 (1990) 91—94.
[43] M. Rubel, R. Haasch, P. Mrozek, A. Wieckowski, C. De Pauli, S. Trasatti, Vacuum 45 (1994) 423—427.
[44] R.S. Chen, H.M. Chang, Y.S. Huang, D.S. Tsai, S. Chattopadhyay, K.H. Chen, J. Cryst. Growth 271 (2004) 105—112.
[45] E.P. Slavcheva, Maced. J. Chem. Chem. Eng. 30 (1) (2011).
[46] J.S. Zhao, J.S. Sim, H.J. Lee, D.-Y. Park, C.S. Hwang, Electrochem. Solid-State Lett. 9 (2006) C29—C31.
[47] C.P. De Pauli, S. Trasatti, J. Electroanal. Chem. 396 (1995) 161—168.
[48] F.-D. Kong, S. Zhang, G.-P. Yin, Z.-B. Wang, C.-Y. Du, G.-Y. Chen, N. Zhang, Int. J. Hydrogen Energy 37 (2012) 59—67.
[49] R. Kötz, H. Neff, S. Stucki, J. Electrochem. Soc. 131 (1984) 72—77.
[50] T.-C. Wen, C.-C. Hu, J. Electrochem. Soc. 139 (1992) 2158—2163.
[51] G. Li, H. Yu, X. Wang, S. Sun, Y. Li, Z. Shao, B. Yi, Phys. Chem. Chem. Phys. 15 (2013) 2858—2866.
[52] A. Marshall, B. Børresen, G. Hagen, S. Sunde, M. Tsypkin, R. Tunold, Russ. J. Electrochem. 42 (2006) 1134—1140.
[53] E. Fachinotti, E. Guerrini, A.C. Tavares, S. Trasatti, J. Electroanal. Chem. 600 (2007) 103—112.
[54] S. Ardizzone, G. Fregonara, S. Trasatti, Electrochim. Acta 35 (1990) 263—267.
[55] G. Li, H. Yu, X. Wang, S. Sun, Y. Li, Z.-G. Shao, B. Yi, Phys. Chem. Chem. Phys. 15 (2012) 2858—2866.
[56] J. Chenga, H. Zhanga, G. Chena, Y. Zhang, Electrochim. Acta 54 (2009) 6250—6256.
[57] L.D. Burke, O.J. Murphy, J. Electroanal. Chem. Interfacial Electrochem. 96 (1979) 19—27.
[58] C. Comninellis, G.P. Vercesi, J. Appl. Electrochem. 21 (1991) 335—345.
[59] L.-E. Owe, M. Tsypkin, S. Sunde, Electrochim. Acta 58 (2011) 231—237.
[60] J.F. Rusling, S.L. Suib, Adv. Mater. 6 (1994) 922—930.
[61] A.A.F. Grupioni, E. Arashiro, T.A.F. Lassali, Electrochim. Acta 48 (2002) 407—418.
[62] Y. Takasu, K. Tsukada, K. Nishimura, T. Hiromine, K. Yahikozawa, Electrochim. Acta 37 (1992) 1029—1031.
[63] S. Siracusano, V. Baglio, A. Di Blasi, N. Briguglio, A. Stassi, R. Ornelas, E. Trifoni, V. Antonucci, A.S. Aricò, Int. J. Hydrogen Energy 35 (2010) 5558—5568.
[64] V.K. Puthiyapura, S. Pasupathi, H. Su, X. Liu, B. Pollet, K. Scott, Int. J. Hydrogen Energy 39 (2014) 1905—1913.